

Optimal location of reinforced inertia to stabilize power grids

Sangjoon Park,¹ Cook Hyun Kim,¹ and B. Kahng¹

¹*CCSS, KI for Grid Modernization, Korea Institute of Energy Technology, Naju, Jeonnam 58330, Korea*

(Dated: February 14, 2025)

The increasing adoption of renewable energy sources has significantly reduced the inertia in the modernized power grid, making the system more vulnerable. One way to stabilize the grid is to add extra inertia from unused turbines, called the fast frequency response (FFR), to the existing grid. However, reinforcing inertia can cause unintended consequences, such as more significant avalanche failures. This phenomenon is known as the Braess paradox. Here, we propose a method to find the optimal position of FFR. This method is applied to the second-order Kuramoto model to find an effective position to mitigate cascading failures. To address this, we propose a method to evaluate a ratio between the positive effects of mitigation and the negative consequences. Through this analysis, we find that the peripheral area of the network is a seemingly effective location for inertia reinforcement across various reinforcement scales. This strategy provides essential insights for enhancing the stability of power grids in a time of widespread renewable energy usage.

I. INTRODUCTION

The power grid is essential for sustaining modern lives, including transportation, healthcare instruments, and food supply. Increasing environmental concerns have recently accelerated the adoption of renewable energy-based power generation systems [1–6]. While this transition reduces dependence on fossil fuels, it has significantly decreased the inertia of power grids, leading to a desperate need for reinforcement strategies [7, 8]. Inertia plays a crucial role in reducing frequency fluctuations before control systems can respond, helping to prevent system instability. Without sufficient inertia, the grid becomes more vulnerable to frequency variations, which can result in large-scale blackouts [9–11].

Various methods have been proposed to enhance the stability of power grids, such as increasing transmission line capacity or connecting new lines. However, these studies have shown that reinforcement may sometimes cause overloads, ultimately reducing grid stability rather than improving it [12–16]. Similarly, while expected to enhance stability, inertia reinforcement may paradoxically exacerbate cascading failures, leading to unintended consequences.

This study investigates how the location and strength of inertia reinforcement affect cascading failure sizes in the second-order Kuramoto model [17]. Our findings reveal that reinforcement can mitigate cascading failures but may also increase their failure size under certain situations. This underscores the importance of identifying optimal reinforcement locations. To evaluate the effects of reinforcement, we measure the ratio of mitigation to adverse outcomes. This ratio decreases as the severity of the Braess paradox increases; however, it increases when mitigation effects are substantial.

By analyzing this ratio across various locations and reinforcement scales, we demonstrate that a topological metric, defined as the combination of mean shortest path length and degree, is a key indicator for identifying optimal reinforcement locations. The results indicate that

this metric exhibits a high Spearman correlation coefficient [18] with the ratio, further supporting its relevance in reinforcement placement. To validate the effectiveness of this topological metric, we classify power plants into three groups based on their metric values: central group, peripheral group, and other group. We then analyze the distribution of the most effective reinforcement locations among these groups to determine which category contains the most optimal reinforcement sites.

The remainder of this paper is organized as follows: Section II introduces the second-order Kuramoto model and the avalanche process. The distribution of cascading failure sizes is obtained for various frequency thresholds. Section III defines inertia reinforcement strategies and examines their mitigation and adverse effects by measuring cascading failures. Section IV proposes a metric for evaluating reinforcement strategies and presents an optimized approach. Finally, Section V provides conclusions and discusses the implications of this study.

II. SECOND-ORDER KURAMOTO MODEL WITH AVALANCHE PROCESS

The second-order Kuramoto model [17] for phase and frequency synchronizations is expressed as follows:

$$m_i \ddot{\theta}_i + \gamma \dot{\theta}_i = P_i + K \sum_{j \in \text{n.n. of } i}^N \sin(\theta_j - \theta_i), \quad (1)$$

where θ_i and $\dot{\theta}_i$ represent the phase and angular velocity of bus i , respectively. The index i denotes the bus index and runs $i = 1, \dots, N$. The parameter m_i and P_i denote the inertia of and power of bus i , respectively. P_i can be positive for generators and negative for consumers. γ is the dissipation coefficient, and K is the coupling strength between neighboring buses. As time passes, the system reaches a steady state where the power at each bus balances with the interaction term.

In the context of power grids, the second-order Kuramoto model is equivalent to the swing equation [19–21],

where K is not constant but depends on the specific buses i and j as $K_{ij} = V_i V_j r_{ij}$. Here, V_i and V_j denote the voltages of buses i and j , respectively, and r_{ij} is the admittance between them. For simplicity, however, we assume $K_{ij} = K$ throughout this study.

In real-world power grids, the frequency of each bus θ_i can fluctuate due to mechanical faults, natural disasters, overload, etc. The frequency fluctuations can trigger cascading failures and large-scale blackouts [22–25]. We consider the avalanche process to account for the cascading failure: (i) Suppose a generator i is malfunctioned. Then $P_i = 0$. It can trigger frequency fluctuations in other buses. (ii) If a θ_j exceeds a given threshold θ_{th} , the bus j is regarded unstable and set systematically $P_j \rightarrow 0$ for maintaining the remaining buses. This process repeats until no further overloaded bus remains. We define the avalanche size s_i as the number of shutdown buses during the cascading failure.

The cascading dynamics depend on the topology of the network [26–29]. Thus, we adopted a real-world network, the UK power grid [22], for our studies. In simulations, on the UK grid topology, we consider the dynamics of the second-order Kuramoto model by using the Runge-Kutta 4th method with a time interval of 10^{-2} seconds. We obtain θ_i and $\dot{\theta}_i$ of each node i . The parameter values are adopted as follows: The intrinsic power P_i of bus i is selected randomly from the Gaussian distribution, in which the elements are confined within the interval $[-8, 8]$, the sum $\sum_i P_i = 0$, and the variance of $\sum_i P_i^2 G(P_i)/N = 9$; Inertia $m = 1$; the dissipation constant $\gamma = 1$; and the coupling strength $K = 60$. Because $\{P_i\}$ are assigned randomly from the Gaussian distribution, the dynamics can vary depending on power configurations $\{P_i\}$. We consider 200 sets of power configurations, and our results are obtained after the ensemble average of those sets. The K value is so large that the system can be regarded as synchronized.

The avalanche size distribution depends on the frequency threshold, θ_{th} . As shown in Fig. 1, the lower threshold generates a bump in the region of large avalanche size, indicating that the system is in a supercritical state. Conversely, higher thresholds lead to subcritical behavior with exponential decay in the tail part. We take $\theta_{th} = 0.3$, at which the avalanche size distribution exhibits a power-law behavior, reflecting a critical behavior [30–33]. At that value, the system exhibits various features, such as diverse avalanche sizes and robust features. Thus, we implement our avalanche dynamics at this critical threshold to obtain a universal behavior from those diverse behaviors.

III. EFFECTS OF INERTIA REINFORCEMENT AND THE BRAESS PARADOX

Many studies have shown that methods intended to improve stability may sometimes trigger the Braess paradox, where improvements lead to unintended adverse

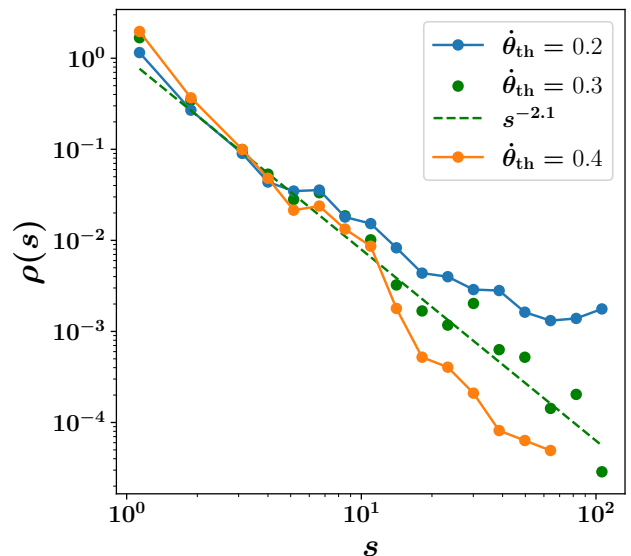


FIG. 1. Avalanche size distribution $\rho(s)$ as a function of avalanche size s for different frequency thresholds θ_{th} in the second-order Kuramoto model. The simulations are implemented on the UK power grid structure with 200 different power configurations. The avalanche size distribution exhibits power-law behavior when the frequency threshold is taken as $\theta_{th} = 0.3$.

effects [12–16]. This section deals with the case where inertia reinforcement can cause unintended adverse consequences. One standard method to reinforce inertia in real-world power grids is to use unused power plant turbines, known as synchronous condensers or fast frequency response (FFR). Specifically, suppose the inertia of generator i ($P_i > 0$) with m_i is increased by m_{FFR} , where m_{FFR} is variable, representing the magnitude of inertia reinforcement.

We analyze the changes in cascading failure size based on the location of additional inertia when a fault occurs at the same power plant. Fig. 2 shows the cascading failure dynamics for $m_{FFR} = 1$. A power plant fault triggers the cascading failures without reinforcing inertia (Fig. 2(a)). Failed nodes are concentrated around the faulted power plant. Next, we examine whether the cascading failure size increases after inertia reinforcement compared to Fig. 2(a). In Fig. 2(b), reinforcement is applied to a node located in the southwestern region. A comparison between Fig. 2(a) and (b) reveals that the number of failed nodes decreases after reinforcement, indicating a mitigating effect. However, when reinforcement is applied at a different location, the cascading failure expands across the entire system, as shown in Fig. 2(c). These results indicate that inertia reinforcement can sometimes lead to adverse effects contrary to general expectations. This highlights the importance of selecting the appropriate reinforcement location to avoid unintended consequences.

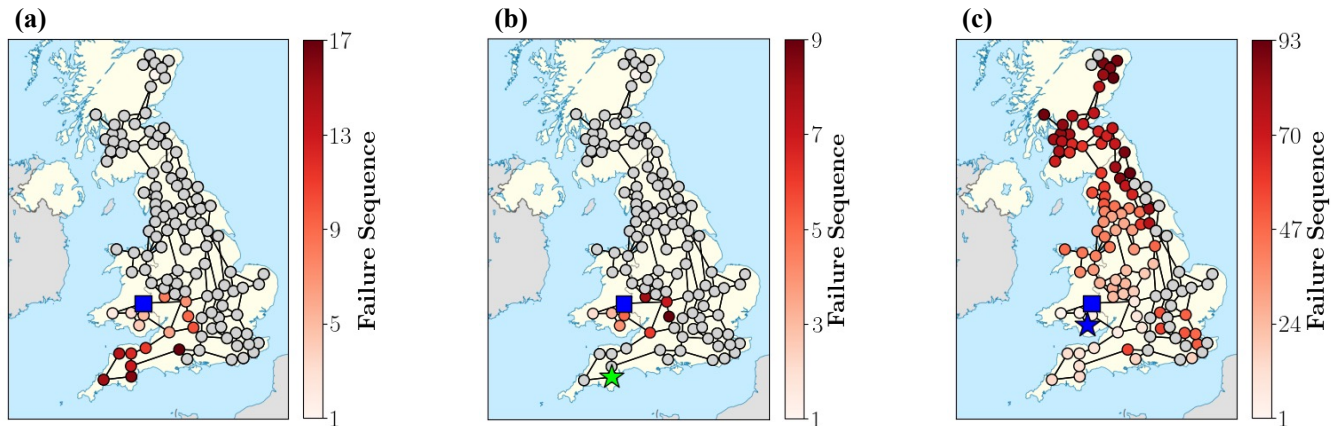


FIG. 2. When a node (■) is fault, frequencies of other nodes change. According to the threshold rule, nodes marked by ● subsequently fail; on the other hand, nodes marked by ○ remain survival. (a) shows the successively failed nodes when inertia reinforcement is absent. (b) shows that when the inertia reinforcement is implemented at (★), the avalanche size is reduced. (c) shows that when the inertia is reinforced by $m_{\text{FFR}} = 1$ at (★), the avalanche size tremendously increases, indicating the Braess paradox.

IV. IDENTIFYING OPTIMAL REINFORCEMENT LOCATIONS

A. Measure for the Effectiveness of Reinforcement

We assess the extent of mitigation and adverse effects that arise at each potential reinforcement site to determine the optimal locations for inertia reinforcement. The cascading failure size, denoted as s , depends on the triggering power plant i locations and the reinforced node k . The change in cascading failure size due to the reinforcement is defined as $\Delta s_i(k) \equiv s_i^{\text{after}}(k) - s_i^{\text{before}}$. When $\Delta s_i(k) < 0$, it indicates that the cascading failure size decreases after reinforcement, signifying successful mitigation. In contrast, $\Delta s_i(k) > 0$ suggests that inertia reinforcement has led to adverse effects, consistent with the Braess paradox. To evaluate reinforcement locations with minimal adverse effects and substantial mitigation, we calculate the ratio $r(k)$ for each node k defined as follows:

$$r(k) = \frac{\sum_{i \in \Delta s_i < 0} |\Delta s_i(k)|}{\sum_{j \in \Delta s_j > 0} \Delta s_j(k)}. \quad (2)$$

This ratio decreases as adverse effects become more significant or mitigation effects weaken. Nodes with higher $r(k)$ values are less vulnerable to the Braess paradox and more stable against cascading failures. Additionally, the reinforcement results are influenced by the power magnitude of the triggering power plant. To account for these variations, $r(k)$ is calculated over 200 ensembles of power configurations.

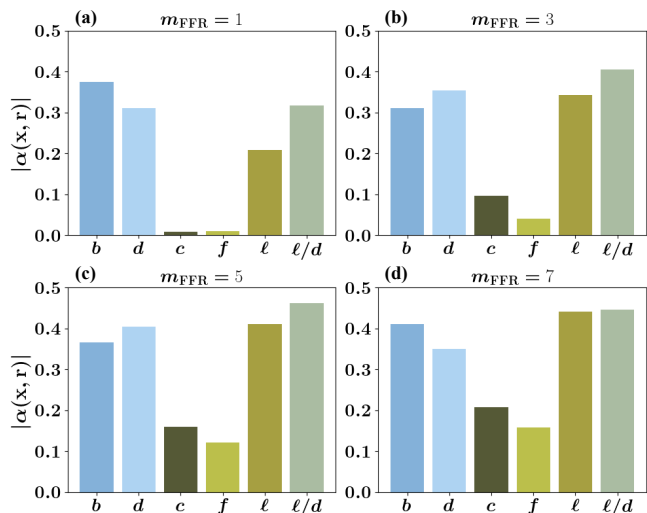


FIG. 3. The magnitude of the Spearman correlation coefficient (a) between \mathbf{r} and network metrics \mathbf{x} of the reinforced node, including betweenness centrality (b), degree (d), clustering coefficient (c), eigenvector components of the Fiedler mode (f), mean shortest path length (ℓ), and the combined metric (ℓ/d). Panels (a), (b), (c), and (d) correspond to reinforcement sizes of $m_{\text{FFR}} = 1, 3, 5, 7$, respectively. Each panel identifies the metric with the highest correlation, highlighting the consistent importance of the combined metric (ℓ/d) across all reinforcement scales.

B. Measure for the Optimal Reinforcement Location

Considering an ensemble of power allocation configurations facilitates the analysis of how the topological properties of reinforcement locations suppress cascading failures. When analyzing a single configuration, it is difficult to determine whether the effectiveness of rein-

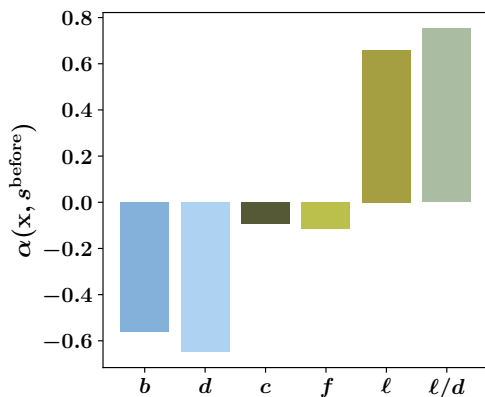


FIG. 4. The Spearman correlation coefficient (α) between various network metrics (\mathbf{x}) and s^{before} . Here, \mathbf{x} represents different network metrics, including betweenness centrality (b), degree (d), clustering coefficient (c), eigenvector components of the Fiedler mode (f), mean shortest path length (ℓ), and the combined metric (ℓ/d). Among these metrics, ℓ/d exhibits the highest positive correlation, indicating that ℓ/d is strongly associated with avalanche sizes. This result underscores the significance of ℓ/d as a key metric for identifying optimal buses for the FFR installment in the network.

forcement is driven by the faulted plant’s power magnitude or by the reinforcement site’s topological effect. However, examining multiple power grid configurations reduces the impact of an initial power plant fault. For instance, if a reinforced power consistently leads to poor outcomes regardless of the fault power magnitude, the site is topologically weak. Therefore, we aim to identify key topological ingredients contributing to effective mitigation by analyzing reinforcement performance across various power grid configurations.

To investigate the topological properties of the most effective reinforcement locations, we measure the Spearman correlation coefficient α between $r(k)$ and various network metrics of the reinforcement node k . The considered metrics include betweenness centrality (b), degree (d), clustering coefficient (c), and the eigenvector components corresponding to the Fiedler mode (f). Additionally, we incorporate the mean shortest path length (ℓ) across all nodes and the combined metric ℓ/d , which accounts for network distance and connectivity. The Spearman correlation coefficient [18] is defined as:

$$\alpha(\mathbf{x}, \mathbf{r}) = \frac{\frac{1}{N} \sum_{k=1}^N (R(r(k)) - \overline{R(\mathbf{r})})(R(x_k) - \overline{R(\mathbf{x})})}{\sqrt{\mathbb{V}(\mathbf{r})\mathbb{V}(\mathbf{x})}}, \quad (3)$$

where $\mathbf{r} = [r(1), r(2), \dots, r(N)]$ and $\mathbf{x} = [x_1, x_2, \dots, x_N]$ represent the vectors of reinforcement effectiveness ratios and the network metrics, respectively. Here, \mathbf{x} represents b, d, c, f, ℓ , or ℓ/d . For instance, if we use betweenness centrality as the network metric, \mathbf{x} becomes $b = [b_1, b_2, \dots, b_N]$. R represents the rank function, \overline{R}

denotes the mean of the ranks, and \mathbb{V} is the variance function.

The Spearman correlation coefficients for different reinforcement sizes ($m_{\text{FFR}} = 1, 3, 5, 7$) are presented in Fig. 3. While b exhibits the highest magnitude of correlation with \mathbf{r} when $m_{\text{FFR}} = 1$, the overall trend suggests that ℓ/d shows the strongest correlation, indicating that a key topological property is crucial for effective inertia reinforcement. To enable significant interactions between the reinforcement bus and other buses, the mean shortest path length should be small, and the degree should be high. Thus, the ratio ℓ/d should be small. The position with high ℓ/d is optimal for installment of FFR. This result is counterintuitive. One may think that the bus with high degree and at the closer distance would be an optimal position; however, the plant at the position is robust due to the sharing load from neighbors plants, and the probability of the bus’s failure is small. In Fig. 4, we measure the Spearman correlation between s^{before} and various network metrics. The results indicate that d negatively correlates with s^{before} , and ℓ/d shows the highest positive correlation. This finding suggests that faults originating in nodes with lower degrees are more likely to trigger larger cascading failures. In other words, areas with many links tend to exhibit greater stability to disturbances than sparse regions. Consequently, reinforcement in robust regions often has minimal impact, as the avalanche size is naturally small, leading to lower $r(k)$ values. In contrast, vulnerable regions provide greater potential for improvement through reinforcement, resulting in higher mitigation effects and, consequently, higher $r(k)$ values.

C. Classification of Effective Reinforcement Locations

To evaluate whether reinforcing nodes with high ℓ_k/d_k values leads to more effective mitigation, we classify power plants into three categories based on their ℓ_k/d_k values in each configuration. As shown in Fig. 5, the top 20 power plants with the highest ℓ_k/d_k values are predominantly located near coastal regions; we refer to this category as the peripheral group. Conversely, the bottom 20 power plants, with the lowest ℓ_k/d_k values, are primarily located in relatively central regions and are designated as the central group. The remaining power plants, which fall between these two extremes, constitute the other category. To assess the effectiveness of this classification, we measure the portion of cases in which the most effective reinforcement locations belong to each group. As shown in Fig. 6, across various reinforcement sizes ($m_{\text{FFR}} = 1, 3, 5, 7$), the majority of reinforcement locations with high $r(k)$ values belong to the peripheral group. This result indicates that irrespective of the power allocation configuration, reinforcing power plants in the regions with high ℓ_k/d_k values consistently leads to lower adverse effects and greater mitigation efficiency.

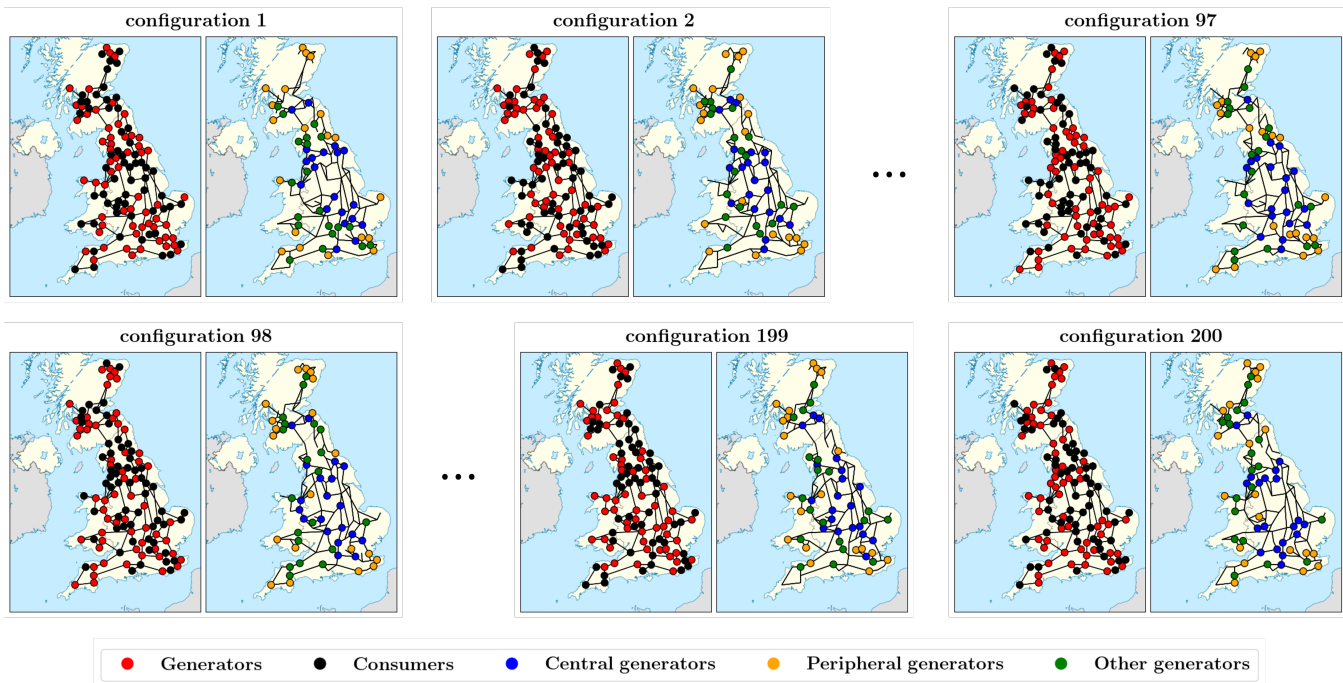


FIG. 5. Classification of power plants into three groups based on their ℓ_k/d_k values across the 200 ensembles of power configurations. The top 20 power plants with the highest ℓ_k/d_k values are categorized as the peripheral group (●), the bottom 20 as the central group (●), and the remaining power plants as the other group (●). Generators (●) and consumers (●) are also shown for reference.

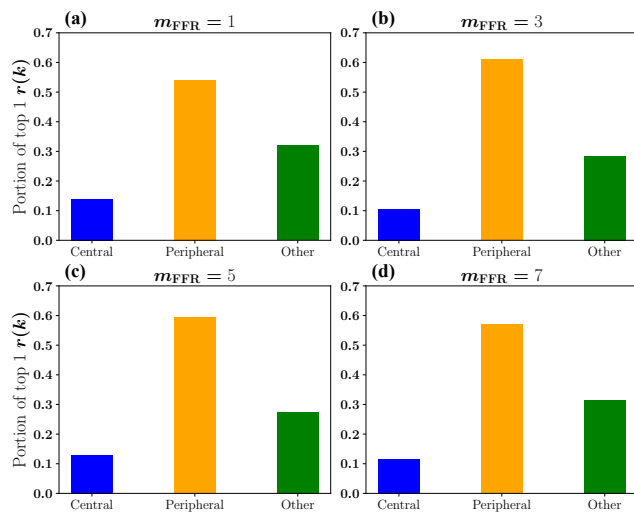


FIG. 6. Portion of power plants in each group (central, peripheral, and other) achieving the highest $r(k)$ across all configurations for different reinforcement sizes. Panels (a)—(d) illustrate that the peripheral group nodes consistently dominate the top-performing locations for $m_{\text{FFR}} = 1, 3, 5, 7$, emphasizing their effectiveness across all reinforcement scales.

V. CONCLUSION

We proposed a method to find the optimal position of the fast frequency response (FFR) installment to reinforce

the inertia in the power grid. As previously remarked, we confirmed the adverse effect called the Braess paradox appears severely in power grids. Even though the inertia of a generator is increased, depending on the position, the cascading failure size can vary, even tremendously huge, leading to a blackout. Thus, finding the optimal position of the FFR is significant. Here, we proposed a system-wide method with the simple synthetic dataset but on actual UK power grid topology, finding the optimal place of the FFR installation.

We analyzed the ratio $r(k)$ to achieve this goal, reflecting mitigation effects and adverse outcomes. Our results show that nodes with high $r(k)$ values are predominantly in peripheral regions. This pattern remains consistent across different reinforcement scales m_{FFR} . Peripheral nodes consistently demonstrate high mitigation effectiveness and minimal adverse effects, highlighting their importance in optimal reinforcement strategies.

As renewable energy-based power plants proliferate, the need for effective inertia reinforcement will grow in future power grids. We anticipate that our proposed strategy will enhance the stability of next-generation grids with similar power generation characteristics.

The second-order Kuramoto model effectively describes the frequency dynamics of power grids. Real-world power grids include threshold frequencies to protect equipment and disconnect nodes when significant frequency deviations occur. We incorporated the avalanche process into the second-order Kuramoto model to reflect this charac-

teristic. Avalanche sizes are determined by the number of nodes exceeding the threshold frequency. As shown in Fig. 1, the threshold frequency θ_{th} significantly influences avalanche dynamics, and we use the value where cascading failure sizes exhibit power-law behavior.

In practical systems, synchronous condensers—idle power plant turbines—are often employed to reinforce inertia [34–36]. We investigated the changes in cascading failures when inertia was reinforced using $m_k \leftarrow m_k + m_{\text{FFR}}$. While inertia reinforcement is generally expected to improve stability, it can occasionally increase the scale of cascading failures, as observed in Fig. 2. To address this, we calculated the ratio $r(k)$ for each reinforcement site k to evaluate both mitigation and adverse effects.

Given that power generation and consumption fluctuate continuously in real-world power systems [37, 38], reinforcement locations determined under a specific power allocation configuration may become suboptimal as power conditions change. However, inertia reinforcement methods like synchronous condensers are not easily relocated in real-time. Therefore, an effective reinforcement strategy must ensure grid stability across varying power allocation configurations.

Since the topological properties of a power grid remain unchanged over time [39, 40], we propose a reinforcement strategy based on network topological metrics. As shown in Fig. 3, ℓ/d exhibits the highest similarity with $r(k)$, establishing it as a reliable indicator for effective reinforcement. This result contrasts with the intuitive expectation that reinforcement should target nodes with a high degree

and short distances to other nodes to maximize influence. In regions with high stability, failures are minimal, and thus, reinforcement is often unnecessary (Fig. 4). Consequently, reinforcing locations that align with intuition results in low $r(k)$ values. This implies that reinforcing topologically vulnerable regions, rather than those with shorter average distances to other nodes, is critical for effective mitigation. To validate the effectiveness of reinforcement based on ℓ/d , we analyze the distribution of the most effective reinforcement locations across different power configurations (Fig. 6). The results reveal that, in most cases, the optimal reinforcement locations are found in the peripheral group, where ℓ_k/d_k values are highest. This finding underscores that reinforcing inertia in peripheral regions represents the most effective strategy for reducing the scale of cascading failures and enhancing overall grid stability.

During the preparation of this work the author(s) used ChatGPT o1 in order to language clarity and readability. After using this tool/service, the author(s) reviewed and edited the content as needed and take(s) full responsibility for the content of the publication.

ACKNOWLEDGMENTS

B.K. was supported by the National Research Foundation of Korea by Grant No. RS-2023-00279802 and the KENTECH Research Grant No. KRG-2021-01-007.

-
- [1] O. Smith, O. Cattell, E. Farcot, R. D. O’Dea, and K. I. Hopcraft, *Science advances* **8**, eabj6734 (2022).
 - [2] F. Dörfler, M. Chertkov, and F. Bullo, *Proceedings of the National Academy of Sciences* **110**, 2005 (2013).
 - [3] A. E. Motter, S. A. Myers, M. Anghel, and T. Nishikawa, *Nature Physics* **9**, 191 (2013).
 - [4] K. Schmietendorf, J. Peinke, and O. Kamps, *The European Physical Journal B* **90**, 1 (2017).
 - [5] Y. Song, C. Wan, X. Hu, H. Qin, and K. Lao, *iEnergy* **1**, 325 (2022).
 - [6] W. Wei, W. Danman, W. Qiuwei, M. Shafie-Khah, and J. P. Catalão, *Journal of Modern Power Systems and Clean Energy* **7**, 433 (2019).
 - [7] K. P. Nnoli and S. Kettemann, *Scientific Reports* **11**, 23742 (2021).
 - [8] L. Rydin Gorjão, R. Jumar, H. Maass, V. Hagenmeyer, G. C. Yalcin, J. Kruse, M. Timme, C. Beck, D. Witthaut, and B. Schäfer, *Nature communications* **11**, 6362 (2020).
 - [9] G. Raman, G. Raman, and J. C.-H. Peng, *Scientific Reports* **12**, 13714 (2022).
 - [10] A. Tayyebi, D. Groß, A. Anta, F. Kupzog, and F. Dörfler, *IEEE Journal of Emerging and Selected Topics in Power Electronics* **8**, 1004 (2020).
 - [11] J. Fritzsche and P. Jacquod, *PRX Energy* **3**, 033003 (2024).
 - [12] L. Pagnier and P. Jacquod, *PloS one* **14**, e0213550 (2019).
 - [13] G. Ódor, I. Papp, K. Benedek, and B. Hartmann, *Physical Review Research* **6**, 013194 (2024).
 - [14] B. Schäfer, T. Pesch, D. Manik, J. Gollenstede, G. Lin, H.-P. Beck, D. Witthaut, and M. Timme, *Nature Communications* **13**, 5396 (2022).
 - [15] T. Coletta and P. Jacquod, *Physical Review E* **93**, 032222 (2016).
 - [16] B. Jhun, H. Choi, Y. Lee, J. Lee, C. H. Kim, and B. Kahng, *Chaos: An Interdisciplinary Journal of Nonlinear Science* **33** (2023).
 - [17] Y. Kuramoto, *Lecture notes in Physics* **30**, 420 (1975).
 - [18] J. L. Myers, A. D. Well, and R. F. Lorch Jr, *Research design and statistical analysis* (Routledge, 2013).
 - [19] G. Ódor, S. Deng, B. Hartmann, and J. Kelling, *Physical Review E* **106**, 034311 (2022).
 - [20] H. Taher, S. Olmi, and E. Schöll, *Physical Review E* **100**, 062306 (2019).
 - [21] G. Ódor and B. Hartmann, *Physical Review E* **98**, 022305 (2018).
 - [22] B. Schäfer, D. Witthaut, M. Timme, and V. Latora, *Nature communications* **9**, 1975 (2018).
 - [23] S. Pahwa, C. Scoglio, and A. Scala, *Scientific reports* **4**, 3694 (2014).
 - [24] L. Daqing, J. Yinan, K. Rui, and S. Havlin, *Scientific reports* **4**, 5381 (2014).
 - [25] Y. Zhang and O. Yağan, *Scientific reports* **6**, 27625 (2016).
 - [26] Y. Yang, T. Nishikawa, and A. E. Motter, *Science* **358**,

- ean3184 (2017).
- [27] M. Rohden, D. Jung, S. Tamrakar, and S. Kettemann, *Physical Review E* **94**, 032209 (2016).
- [28] D. Witthaut and M. Timme, *Physical Review E* **92**, 032809 (2015).
- [29] M. Turalska, K. Burghardt, M. Rohden, A. Swami, and R. M. D'Souza, *Physical Review E* **99**, 032308 (2019).
- [30] B. A. Carreras, D. E. Newman, I. Dobson, and A. B. Poole, *IEEE Transactions on Circuits and Systems I: Regular Papers* **51**, 1733 (2004).
- [31] B. A. Carreras, D. E. Newman, and I. Dobson, *IEEE Transactions on Power Systems* **31**, 4406 (2016).
- [32] I. Dobson, B. A. Carreras, V. E. Lynch, and D. E. Newman, *Chaos: An Interdisciplinary Journal of Nonlinear Science* **17** (2007).
- [33] B. A. Carreras, V. E. Lynch, I. Dobson, and D. E. Newman, *Chaos: An Interdisciplinary Journal of Nonlinear Science* **14**, 643 (2004).
- [34] H. T. Nguyen, G. Yang, A. H. Nielsen, and P. H. Jensen, *IEEE Transactions on Sustainable Energy* **10**, 997 (2018).
- [35] V. Arayamparambil Vinaya Mohanan, I. M. Mareels, R. J. Evans, and R. R. Kolluri, *IET Generation, Transmission & Distribution* **14**, 3582 (2020).
- [36] H. T. Nguyen, G. Yang, A. H. Nielsen, P. H. Jensen, and B. Pal, *Journal of Modern Power Systems and Clean Energy* **9**, 639 (2020).
- [37] S. Javaid, M. Kaneko, and Y. Tan, *IEEE Access* (2024).
- [38] Y. Tang, J. Zhong, and J. Liu, *IEEE Transactions on Power Systems* **31**, 125 (2015).
- [39] N. Komendantova and A. Battaglioni, *IEEE Power and Energy Magazine* **14**, 79 (2016).
- [40] O. Ziaee and F. F. Choobineh, *IEEE Transactions on Power Systems* **32**, 94 (2016).